https://doi.org/10.1016/j.cej.2018.06.031

Novel three dimensional hierarchical porous Sn-Ni alloys as anode for lithium ion batteries with long cycle life by pulse electrodeposition

Xin Dong,[1,a] Wenbo Liu,[1,a,b,*] Xue Chen,[a] Jiazhen Yan,[a] Ning Li,[a] Sanqiang Shi,[b] Shichao Zhang,[c] and Xusheng Yang[d]

[a] School of Manufacturing Science and Engineering, Sichuan University, Chengdu 610065, China

[b] Department of Mechanical Engineering, The Hong Kong Polytechnic University, Hung Hom, Kowloon, Hong Kong

[c] School of Materials Science and Engineering, Beihang University, Beijing 100191, China

[d] Department of Industrial and Systems Engineering, The Hong Kong Polytechnic University, Hung Hom, Kowloon, Hong Kong

[1] These authors contributed equally.

Tel: +86-028-85405320; Fax: +86-028-85403408; E-mail: liuwenbo_8338@163.com.

Abstract

In this paper, novel three dimensional hierarchical porous Sn-Ni (3D-HP Sn-Ni) alloys were investigated as a promising anode for high-performance Li ion batteries (LIBs), which was fabricated by pulse electrodeposition of mesoporous Sn-Ni alloy made of ultrafine nanoparticles on the 3D nanoporous copper substrate from chemical dealloying of as-cast $Al_{55}Cu_{45}$ (at.%) alloy slices in the HCl solution. The results show that the as-obtained 3D-HP Sn-Ni alloys are typically characteristic of open, bicontinuous, interpenetrating bimodal pore size distribution comprising large-sized (hundreds of nm) ligament-channel network architecture with highly porous channel walls (several nm). Compared to the two dimensional nanoporous Sn-Ni (2D-NP Sn-Ni) thin films, the 3D-HP Sn-Ni alloys as anode for LIBs show superior cycling stability with reversible specific capacity of 0.25 mAh cm^{-2} and coulombic efficiency of more than 95% upto 200 cycles. Moreover, the reversible capacity as high as 0.22 mAh cm^{-2} can be achieved even after a series of high-rate charge-discharge cyclings. The satisfactory electrochemical properties can be mainly ascribed to the unique 3D hierarchical porous structure, large contact surface area between active material and electrolyte, as well as good buffer effect of inactive component, which is greatly beneficial to alleviate the huge volume variation, enhance the loading mass of active material, shorten the Li^+ migration distance and improve the electron conductivity. We believe that this present work can provide a promising anode candidate towards practical application of high-performance LIBs.

***Keywords*:** Lithium ion battery; Sn-Ni alloy; Hierarchical porous structure; Pulse

electrodeposition; Anode

1. Introduction

Nowadays, LIBs have become the primary power device for portable electronic products. Typically, the rapid development of pure/hybrid electric vehicles has put forward an urgent demand for LIBs with higher energy density and longer cycle life [1, 2]. Unfortunately, their further improvements are severely hindered by traditional graphite anode due to the relatively low theoretical specific capacity (~372 mAh g^{-1}) and markedly low Li-insertion potential (close to the deposition potential of metal Li). Therefore, it is urgent for us to search for alternative anode materials with higher theoretical capacity and more proper lithiation potential to meet the demands for next-generation LIBs. In recent years, tin has been increasingly recognized as an ideal anode candidate to potentially replace graphite in advanced LIBs, thanks to its high theoretical capacity (994 mAh g^{-1}), environmentally friendly and abundant reserves in earth's crust [3-5]. However, the key challenge to prevent tin from practical utilization is its huge volume variation during charge-discharge processes, easily resulting in the fast pulverization, mechanical disintegration and terrible cycling performance [6-9].

A substantial of research efforts have been devoted to surmount the obstacles with the final objective to achieve tin efficient utilization and enhance its cycle life. Among them, the rational structure and composition design of tin anode to accommodate the volume variation is proved to be effective pronouncedly [3-13]. On one hand, various nanostructures gained considerable attention and exploration, such as nanorods [15-17], nanotubes [18-20], nanospheres [11, 21] and nanoporous structures [22-28]. The primary goal to use these nanostructures was to effectively alleviate the huge

volume change in the process of lithiation/de-lithiation, and increase the contact area between electrode and electrolyte for enhanced electrochemical reaction. On the other hand, introducing inactive components to build active/inactive composite system is also an effective approach to improve tin's electrochemical property [5, 29-31]. Evidently, it can buffer the volume expansion and particle aggregation of tin during repeated cyclings because inactive components can serve as cushions to relax the mechanical stress during the lithiation/de-lithiation processes. Among various tin-inactive species, Sn-Ni alloy has received increasingly attention due to its excellent physicochemical property, matching attribute and cushioning effect. Typically, Bruno Scrosati et al. reported the Ni_3Sn_4 anode with nanorod arrays exhibiting the high specific capacity of 500 mAh g^{-1} at the 200th cycle through a template synthesis procedure [29]. The 3D porous reticular Sn-Ni alloy prepared by Ling Huang et al. [12] delivered a reversible specific capacity as high as 501 mAh g^{-1} after 50 cycles of charge-discharge. Additionally, the porous Sn-Ni alloy dendrites synthesized by a facile constant-current deposition method showed the high charge capacity of 530 mAh g^{-1} after 50 cycles [26].

Inspired by these, it could be reasonable to believe that combining nanostructures and active/inactive system might be a more valid route to obtain enhanced Li-storage property. Among various nanostructures, 3D nanoporous structure has itself unique advantages towards LIBs application relative to ordinary 1D and 2D nanostructures, such as rigid 3D framework, large surface area, high active sites and fast ion/electron transport. Most recently, dealloying has been evidenced to be a facile and effective

approach to construct different kinds of 3D nanoporous structures, which possesses significant advantages of simple processing, nearly absolute yield, and being applicable for large-scale synthesis relative to other strategies reported in the literature [32-35].

Herein, novel 3D-HP Sn-Ni alloy anode was synthesized by pulse electrodeposition of mesoporous Sn-Ni alloy made of ultrafine nanoparticles on the 3D nanoporous copper substrate from chemical dealloying of $Al_{55}Cu_{45}$ alloy slices in the HCl solution. The as-prepared 3D-HP Sn-Ni anode is typically characteristic of open, bicontinuous, interpenetrating bimodal pore size distribution comprising interconnected large-sized ligament-channel networks with highly porous channel walls. Compared to the 2D-NP Sn-Ni thin films, the 3D-HP Sn-Ni electrode exhibited superior cycling stability with reversible specific capacity of 0.25 mAh cm^{-2} and coulombic efficiency of >95% upto the 200th cycle, which is likely related to the unique 3D hierarchical porous structure, large contact area between active material and electrolyte, as well as favourable buffer effect of inactive component. We believe that this work can provide a promising anode candidate towards practical application of high-performance LIBs.

2. Experimental section

2.1. Preparation of 3D-HP Sn-Ni and 2D-NP Sn-Ni alloys

Figure 1 illustrates the synthetic schemes of 3D-HP Sn-Ni and 2D-NP Sn-Ni alloys. In the typical fabrication process of 3D-HP Sn-Ni alloys, Al-Cu ingots with nominal composition of $Al_{55}Cu_{45}$ (at.%) were prepared firstly from pure aluminum (99.9 wt.%) and pure copper (99.99 wt.%) by vacuum induction furnace. Then, Al-Cu ingots were

sliced into sheets with 400 μm in thickness by wire-cutting EDM, which subsequently were ground and polished to remove oxide layers on the surfaces. Energy dispersive X-ray (EDX) analysis showed the atomic percentage of Cu and Al in the Al-Cu slices was quite closely to the initial designed composition, indicating that the alloy slices can be further used in the following study (see supplementary material for the detailed EDX results, Figure S1). Whereafter, the Al-Cu alloy slices were put into 5wt.% HCl solution to be subjected to chemically dealloy at 90℃ for 5 hrs, upon which the samples were rinsed with distilled water and ethanol for several times. Finally, the 3D nanoporous copper (NPC) substrate can be obtained after dried at 70℃ for 24 hrs in vacuum oven. The final thickness of the 3D NPC substrate was ca. 230 μm.

Subsequently, the Sn-Ni nanoparticles were electroplated on the NPC substrates to fabricate the 3D-HP Sn-Ni alloys. Note that pulse current as control variable was utilized in the process of electroplation, because: (1) the current density with periodic changes can easily produce fine nanoparticles and integrated plating layers, (2) the morphology, sizes and amount of deposits can be controlled easily, (3) there is no need of anyother conductive agent and binder. Pulse electrodeposition was performed using an electrochemical measurement unit (CHI760E, CH Instruments, Inc.) in a standard three-electrode electrochemical cell (100 mL) with the 3D NPC substrate as working electrode, Pt foil as counter electrode and saturated calomel electrode (SCE) as reference electrode. The detailed technical parameters of pulse electrodeposition can be found in Figure S2. The plating bath was composed of $NiCl_2 \cdot 6H_2O$ 14.67 g/L, $SnCl_2 \cdot 2H_2O$ 46 g/L, $C_4O_6H_4KNa$ 8 g/L, $K_4P_2O_7$ 300 g/L, and glycine 8 g/L [29]. The

typical reaction duration was 2-3 min, and the as-obtained 3D-HP Sn-Ni alloys were washed mildly and dried at 75℃ for 20 hrs in vacuum oven. For comparison, the 2D-NP Sn-Ni alloys were fabricated by pulse electrodeposition onto the 2D planar copper foil (2D CF) substrates under the same conditions. The typical thickness of the 2D CF substrate was 200 μm. Note that all areas in this work referred to foot print areas and all used chemical reagents were analytical grade.

2.2. Structure and composition characterizations

Microstructure and chemical composition of the resultant specimens were detected by field-emission scanning electron microscopy (FESEM，Hitachi S-4800) with an EDX analyzer, transmission electron microscopy (TEM and HRTEM, JEOL JEM 2100F). Crystalline phases were analyzed using X-ray diffraction (XRD, Rigaku D/Max-2400) with Cu K_α radiation from 20° to 80°.

2.3. Electrochemical test

The as-prepared 3D-HP Sn-Ni and 2D-NP Sn-Ni alloys as working electrodes, respectively, were assembled into coin-type test cells (CR2032) in an argon-filled glove box (LS-750D, DELLIX) with metal Li as counter and reference electrodes, 1 M $LiPF_6$ in a mixture of ethylene carbonate/diethyl carbonate (1:1 v/v) as electrolyte, and polypropylene film (Celgard 2400) as separator. Each cell was aged for 24 hrs at room temperature before commencing the electrochemical tests. The half-cells were charged and discharged galvanostatically on a multichannel battery test system (NEWARE BTS-610, Neware Technology Co., Ltd., China) between 0.01 and 1.5 V(vs. Li/Li^+) at room temperature. Cyclic voltammograms (CVs) was recorded using

a CHI760E electrochemical workstation at a scan rate of 0.1 mV s^{-1} between 0.01 and 1.5 V (vs. Li/Li^+). Electrochemical impedance spectroscopy (EIS) measurements were carried out over a frequency range from 0.01 Hz to 1 MHz with AC amplitude of 5 mV.

3. Results and discussion

3.1. Morphology and structure characterization

Figure 2a and b shows the SEM images of surface morphology of as-prepared 3D NPC substrate by chemical dealloying of $Al_{55}Cu_{45}$ alloy slice in the HCl solution. It is clear that the NPC substrate exhibits an open, bicontinuous, interpenetrating porous network structure with uniformly large pore/ligament sizes of 350±150 nm. Also, the cross-section SEM images of the NPC substrate from Figure S3 further verify the 3D porous network characteristic, which would be greatly beneficial for the infiltration of electrolyte in the subsequent pulse electrodeposition. Figure 2c displays the microstructure of 3D-HP Sn-Ni electrode by pulse electrodeposition under the mild reaction condition. Apparently, the large-sized porous skeleton of the 3D-HP electrode well inherits that of the NPC substrate, and meanwhile no obvious structure change and pore blocking can be observed, indicative of favourable 3D channels for mass transfer. It is worthwhile noting that, from Figure 2d and its high-magnification inset, the large-sized ligament surface of 3D-HP Sn-Ni electrode further exhibits the uniform mesoporous architecture composed of ultrafine nanoparticles with mean sizes of 3-5 nm, finally resulting in the formantion of unique 3D hierarchical porous structure. Furthermore, the typical TEM and HRTEM observations from Figure 2g

and h confirm the hierarchical porous structure of 3D-HP Sn-Ni electrode; meanwhile, HRTEM analysis also shows the lattice fringe spacing of the deposited ultrafine nanoparticles is 2.95 Å, corresponding to the (111) plane of Ni_3Sn_4. Additionally, the element content of 3D-HP Sn-Ni electrode has been determined by EDX measurement to be Sn/Ni≈31:19 (at.%), and the deposition amount and element proportion can be easily tuned by simply changing the plating time and eletrolyte concentration. The EDX mapping results of Sn, Ni and Cu elements exhibit uniform distribution of Ni and Sn on the whole 3D NPC substrate (Figure S4), which would be beneficial to prevent active material from cracking and detachment from current collector during repeated charge-discharge processes. For comparison, the microstructure and surface morphology of 2D-NP Sn-Ni electrode by pulse electrodeposition on the 2D CF substrate under the same deposition conditions exhibit an open, irregular, discontinuous nanoporous structure with mean pore/ligament sizes of 30-80 nm, as presented in Figure 2e and f. The EDX analysis further reveals that the content ratio of Sn and Ni elements is approximately 14:1 for the 2D-NP Sn-Ni electrode.

Figure 3 displays the XRD spectra of as-prepared 3D NPC substrate, 3D-HP Sn-Ni and 2D-NP Sn-Ni electrodes. As can be seen clearly from Figure 3a, the diffraction peaks at 2θ=43.29°, 50.43°, and 74.14° correspond to f.c.c $(111)_{Cu}$, $(200)_{Cu}$ and $(220)_{Cu}$, indicative of the exact existence of single Cu phase. For the 3D-HP Sn-Ni electrode (Figure 3b), the Ni_3Sn_4 phase can be detected at 2θ=30.27° other than those belonging to NPC substrate, suggesting that Ni_3Sn_4 is the only deposition after pulse

electrodeposition on the 3D substrate, which is in good agreement with the HRTEM analysis. In contrast, the Cu, Ni_3Sn_4, Sn phases can be indexed simultaneously in the 2D-NP Sn-Ni electrode by pulse electrodeposition on the 2D CF substrate under the same conditions. Note that the single Sn phase can be obtained just in the 2D-NP electrode compared to the 3D-HP one, implying that the surface morphology and microstructure of substrate plays a crucial part in the phase composition and content of deposition. This is likely related to the sizes of specific surface area and the amount of active sites on substrates with different morphologies, which has been discussed detailedly in the following part on a basis of CV results.

To further reveal the electrodeposition mechanisms, the CVs were measured during depositions onto the 2D CF and 3D NPC substrates from -0.4 to -1.4 V(vs. SCE) in the different bath solutions containing separate Ni^{2+}, Sn^{2+} and the mixture of Ni^{2+} and Sn^{2+}, respectively (Figure 4). As is well-known, the emergence of some reduction peak in CVs corresponds to the deposition of a metal as the potential scans towards the negative direction, in which the reduction peak area stands for deposition amount. Note that the reduction process of Ni^{2+} to Ni is obviously different between the 2D CF and 3D NPC substrates relative to Sn^{2+}, as shown in the curves 2 of Figure 4, indicating that the electrodeposition behavior of metal Ni is greatly susceptible to the microstructure and surface morphology of substrate. Moreover, it can be found from the reduction peak areas that the loading mass of metal Ni on the 3D porous substrate is much more than that on the 2D planar one, which is in line with the EDX results in Figure 2. This is closely associated with the large specific surface area and high active

sites (e.g. plenty of 2D and 3D surface defects) of the unique 3D NPC substrate obtained by dealloying, which might be much favorable for nucleation and growth of metal Ni by electrodeposition [36-38]. Analogously, from the curves 3 of Figure 4, it can be understood that the electrodeposition behavior of metal Sn is less sensitive to the microstructure and surface morphology of substrate than metal Ni, and thus the loading mass of Sn on the 3D porous substrate is just comparable to that on the 2D planar substrate. As a result, a number of Sn-Ni alloys can be obtained by pulse electrodeposition onto the 3D substrate, while just a few Sn-Ni alloys and relatively more single Sn can be formed on the 2D counterpart. This is also in good accordance with the results of curves 1 in Figure 4. It should be noted that, however, the fact that the more Sn obtained in the 3D-HP electrode seems to be paradoxical with the present XRD results, which exactly displays the higher Sn contents in the 2D-NP electrode. We consider that this illusion would be mainly related to the detection limit depth (just 10^2~10^3 nm) of characteristic X-ray from XRD instrument, which is far less than the thickness (~250 μm) of the present 3D-HP Ni-Sn electrode. To confirm it, the SEM observation and EDX analysis of cross-sections of 3D-HP Sn-Ni electrode was further performed, as displayed in Figure S5. Obviously, the microstructure and chemical composition of cross-sections of the 3D porous specimens are highly identical to those from their surfaces in Figure 2, indicating that the mesoporous Sn-Ni alloy well covers the 3D porous skeleton of substrates rather than just on the surfaces.

3.2. Electrochemical properties

The lithium storage mechanism of 3D-HP Sn-Ni electrode during charge-discharge processes can be investigated by cyclic voltammetry. It has been reported in the literature that the electrochemical lithiation/de-lithiation processes of Sn-Ni alloy involves main three reaction steps as follows: The step (1) is deemed to be irreversible activation process in order to convert Sn-Ni alloy into Li_xSn/Ni ($0<x<4.4$) composite; the steps (2-3) are two reversible electrochemical reaction processes corresponding to alloying/dealloying between Li and Sn, which has been elucidated detailedly in the previous studies [24, 25].

$$Ni_mSn_n + xnLi^+ + xne^- \rightarrow nLi_xSn + mNi \ (0<x<4.4) \quad (1)$$

$$Sn + xLi^+ + xe^- \rightarrow Li_xSn \ (0<x<4.4, \text{discharge}) \quad (2)$$

$$Li_xSn \rightarrow Sn + xLi^+ + xe^- \ (0<x<4.4, \text{charge}) \quad (3)$$

Figure 5a shows the first three-cycle CVs of 3D-HP Sn-Ni electrode at a scan rate of 0.1 mV s^{-1}. Clearly, three broad cathodic peaks can be observed around 1.0, 0.4 and 0.2 V(vs. Li/Li^+), respectively. The peaks at 1.0 and 0.4 V(vs. Li/Li^+) can be attributed to the formation of a solid electrolyte interface (SEI) and irreversible conversion of Sn-Ni alloy to Sn/Ni composite indicated by Equation (1). Note that these two peaks disappeared in the subsequent cycles, implying the stability of SEI and the entire conversion of Sn-Ni alloy to Sn/Ni composite. The cathodic peak at 0.2 V(vs. Li/Li^+) can be ascribed to the formation of Li_xSn ($0<x<4.4$) alloy as described by Equation (2). During the 1st charge process, the two anodic peaks emerging at 0.56 and 1.2 V(vs. Li/Li^+) correspond to the reversible electrochemical reactions of Li_xSn to Sn as presented by Equation (3). It is worth noting that the subsequent cycle curves are well

overlapped with each other, clearly demonstrating its excellent cycling stability and electrochemical reversibility.

The voltage vs. capacity profiles of 3D-HP Sn-Ni electrode are also recorded at a current density of 0.1 mA cm^{-2}, as indicated in Figure 5b. As can be seen clearly, the first discharge and charge processes delivered the large specific capacities of 0.96 and 0.49 mAh cm^{-2}, respectively, with a relatively high coulombic efficiency beyond 51%. The initial capacity loses mainly can be assigned to the irreversible conversion of Sn-Ni alloy and formation of SEI [11, 23]. It should be noted that the plateaus at 1.0 and 0.4 V(vs. Li/Li^{+}) relating to the two irreversible reactions in the 1st discharge process disappeared afterwards and the 2nd charge-discharge curve overlapped well with that in the 3rd cycle, which also are in good accordance with the CVs in Figure 5a.

Figure 5c illustrates the cycle performance of 3D-HP Sn-Ni electrode at a current density of 0.1 mA cm^{-2}; meanwhile, the counterpart of 2D-NP Sn-Ni electrode is also added for clear comparison. Compared to the 2D-NP electrode, the as-prepared 3D-HP Sn-Ni electrode exhibits the significantly improved cycling ability with higher specific capacity, longer cycle life and more steady coulombic efficiency, indicating that the 3D porous substrate plays a key part in accommodating the huge volume variation and enhancing the loading mass of active material. Note that after a slight decrease of specific capacity in the initial several cycles, the 3D-HP Sn-Ni electrode retains excellent cycling stability and no obvious capacity loses occur in the subsequent cycling processes upto the 200th cycle. The reversible capacity retention

of 3D-HP Sn-Ni electrode reaches 69.7% after first 10 cycles and still can maintain beyond 51% after 200 cycles. Except for the first several cycles, its coulombic efficiency always maintains above 95%, indicative of the superior electrochemical reversibility. Typically, the reversible capacities of 0.31, 0.29 and 0.27 mAh cm^{-2} can be reached at the 20th, 50th and 120th cycles for 3D-HP Sn-Ni electrode, respectively. Even after 200 cycles, it still can deliver a relatively high reversible capacity of 0.25 mAh cm^{-2}. In contrast, the reversible capacities of 0.11 and 0.04 mAh cm^{-2} can be attained only for the 2D-NP Sn-Ni electrode at the 20th and 50th cycles, respectively. Obviously, the areal specific capacity of 2D-NP Sn-Ni electrode sharply decreased from the beginning and only 24% capacity retention remains at the 50th cycle. Such a low capacity retention can be main relation to the uneven, discontinuous nanoporous structure and relatively low content of inactive component Ni as cushion, which would lead to the insufficient accommodation of huge volume change from Sn during lithiation/de-lithiation processes and rapid detachment from the 2D CF substrate. In addition, the cycle performance and coulombic efficiency of 3D-HP Sn-Ni and 2D-NP Sn-Ni electrodes have been expressed further by mass capacity in order to effectively compare with other Sn-based electrode materials reported in the literature, as present in Figure S6. Obviously, the better cycling stability and longer cycle life can be obtained in the 3D-HP Sn-Ni electrode (Table S1).

Rate capacity profiles of 3D-HP Sn-Ni electrode at the different current densities were further measured, as displayed in Figure 5d. It is clear that as the current density reaches 0.3 and 0.4 mA cm^{-2}, the 3D-HP Sn-Ni electrode can maintain the high

reversible capacities of 0.24 and 0.22 mAh cm^{-2}. When the current density returned to 0.1 mA cm^{-2} at the 50th cycle, the reversible capacity increases to 0.28 mAh cm^{-2}, which reserves as high as 84.8% capacity retention compared with the 10th cycle at the same current density. It is worth noting that after undergoing a series of high-rate charge-discharge processes, the reversible capacity still can maintain 0.22 mAh cm^{-2} in the 200th cycle, demonstrating its excellence for rate performance. This can be mainly ascribed to the unique 3D hierarchical porous structure, which can not only endow the better electrolyte permeation, but also provide the larger contact areas between electrode and electrolyte. In addition, the nanoscaled Sn-Ni composite system can effectively withstand the large volume changes and shorten the Li^+ diffusion paths during repeated charge-discharge processes.

The ion and electron transports of 3D-HP Sn-Ni and 2D-NP Sn-Ni electrodes were investigated by EIS, as depicted in Figure 6, which is one of the most important methods to reveal the Li^+ and electron transport kinetics at the electrode/electrolyte and current collector/active material interfaces in LIBs. As indicated in Figure 6, both Nyquist plots consisted of a semicircle in high to medium frequency range, the diameter of which represented the charge transfer resistance and an inclined line in the low frequency range closely related to the diffusion coefficient of Li^+ inside electrode materials [39]. Note that the 3D-HP Sn-Ni electrode has markedly low charge transfer resistance (R_{ct}≈50 Ω) at the initial state compared to that (R_{ct}≈800 Ω) of 2D-NP Sn-Ni electrode. It is exciting that the charge transfer resistance of 3D-HP electrode still has no sharp increase after 50 (R_{ct}≈70 Ω) and 200 cycles (R_{ct}≈110 Ω), implying its

excellent electron conductivity. On the contrary, the diameter of the semicircle for 2D-NP electrode abruptly enlarges just after 50 cycles (R_{ct}>1000 Ω), suggesting the remarkably poor electrochemical property. In order to understand it quantitatively, the fitting curves and equivalent circuits of EIS of 3D-HP Sn-Ni and 2D-NP Sn-Ni electrodes after 50 cycles have been achieved in Figure S7. Evidently, the R_{ct} value of 3D-HP Sn-Ni electrode is just 69 Ω, which is far lower than that of 2D-NP Sn-Ni electrode (1030 Ω). The present results clearly demonstrate that the unique 3D-HP Sn-Ni alloy as anode for LIBs possesses much better Li^+ and electron transport abilities.

Figure 7 shows the SEM images of 2D-NP Sn-Ni and 3D-HP Sn-Ni electrodes after cyclings. Obviously, for the 2D-NP Sn-Ni electrode after 50 cycles, several irregular clusters comprising aggregated nanoparticles and uneven large pits from pulverization and detachment of active material can be observed in Figure 7a and its inset, which is closely associated with the huge volume variation and inadequate structure buffering during charge-discharge processes. Note that the present microstructure and surface morphology are quite different from its original state in Figure 2e-f. Especially, the random orientation of ligaments and pores after cyclings clearly demonstrates the 2D planar substrate cannot buffer the huge volume change effectively during repeated lithiation/de-lithiation processes, finally resulting in the terrible electrochemical behavior. In stark contrast, the microstructure and surface morphology of 3D-HP Sn-Ni electrode after 50 cycles were presented in Figure 7b. It can be found easily that no obvious difference exists before and after cyclings. The high-magnification

SEM image in the inset of Figure 7b further exhibits that the Sn-Ni nanoparticles still are anchored well on the 3D porous skeleton and no obvious aggregation occurs after 50 cycles, indicating the favourable binding force between active material and 3D substrate. This is mainly because the 3D Sn-Ni electrode with unique hierarchical porous architecture provides ample spaces for alleviation of volume expansion and abundant active sites for growth of active material. In order to further testify the superiority of as-prepared 3D-HP Sn-Ni electrode, its microstructure after 200 cycles was also characterized in Figure 7c. It is astonishing that the nearly perface 3D hierarchical porous structure still can be seen clearly and no obvious cracking, pulverization and detachment of active material occur from the 3D NPC substrate even after such a long charge-discharge cycle, demonstrating its promising application for high-performance LIBs.

4. Conclusions

The novel three dimensional hierarchical porous Sn-Ni alloys as anode for LIBs has been fabricated successfully by pulse electrodeposition of mesoporous Sn-Ni alloy made of ultrafine nanoparticles on the 3D NPC substrates from chemical dealloying of as-cast $Al_{55}Cu_{45}$ (at.%) alloy slices in the HCl solution. The unique 3D-HP Sn-Ni anodes possess typically open, bicontinuous, interpenetrating bimodal pore size distribution comprising interconnected large-sized (hundreds of nm) ligament-channel structure with highly porous channel walls (several nm). Compared with the 2D-NP Sn-Ni one, the 3D-HP Sn-Ni electrode exhibits remarkably higher reversible capacity (0.49 mAh cm^{-2} at the 1st cycle), longer cycling stability (>51% capacity retention

after 200 cycles) and better rate capacity (0.22 mAh cm^{-2} at the 0.4 mA cm^{-2}). The excellent electrochemical property can be mainly attributed to the 3D hierarchical porous structure, large specific surface area and good buffer effect of inactive component, which plays an important role in alleviating the huge volume variation during charge-discharge processes, raising the loading mass of active material and accelerating the Li^+ diffusion and electron transport. We believe that the high specific capacity, long cycle life, steady coulombic efficiency, low preparation cost and easy large-scale production of the 3D-HP electrode will open up a brand-new opportunity to develop the promising anode candidate for high-performance LIBs.

Acknowledgements

We give thanks to financial support by the National Natural Science Foundation of China (51604177), the State Key Basic Research Program of PRC (2013CB934001), the Hong Kong Scholars Program (XJ2014045, G-YZ67), the China Postdoctoral Science Foundation (2015M570784), the International S&T Cooperation and Exchange Program of Sichuan Province (2017HH0068), the Scientific Research Fund of Sichuan Provincial Department of Education (16ZB0002), the Experimental Technology Project of Sichuan University (20170133), the “1000 Talents Plan” of Sichuan Province, the Fundamental Research Funds for the Central Universities, and the Talent Introduction Program of Sichuan University (YJ201410).

Supplementary material available: Figures S1-S7 and Table S1. This material is available free of charge via the Internet at http://www.elsevier.com.

References

[1] J.-M. Tarascon, M. Armand, Issues and challenges facing rechargeable lithium batteries, Nature 414 (2001) 359-367.

[2] M. Armand, J.-M. Tarascon, Building better batteries, Nature 451 (2008) 652-657.

[3] S.C. Zhang, Y.L. Xing, T. Jiang, Z.J. Du, F. Li, L. He, W.B. Liu, A three-dimensional tin-coated nanoporous copper for lithium-ion battery anodes, J. Power Sources 196 (2011) 6915-6919.

[4] Y. Yu, L. Gu, X.Y. Lang, C.B Zhu, T. Fujita, M.W. Chen, J. Maier, Li storage in 3D nanoporous Au-supported nanocrystalline tin, Adv. Mater. 23(21) (2011) 2443-2447.

[5] X.S. Zhou, Z.H. Dai, S.H. Liu, J.C. Bao, Y.G. Guo, Ultra-uniform SnO_x/carbon nanohybrids toward advanced lithium-ion battery anodes, Adv. Mater. 26(23) (2014) 3943-3949.

[6] S. Javadian, J. Kakemam, A. Sadeghi, H. Gharibi, Pulsed current electrodeposition parameters to control the Sn particle size to enhance electrochemical performance as anode material in lithium ion batteries, Surf. Coat. Tec. 305 (2016) 41-48.

[7] D. Zhou, W.L Song, X. Li, L.Z. Fan, Y. Deng, Tin nanoparticles embedded in porous N-doped graphene-like carbon network as high-performance anode material for lithium-ion batteries, J. Alloys Compd. 699 (2016) 730-737.

[8] Y. Yu, C.H. Chen, Y. Shi, A tin-based amorphous oxide composite with a porous, spherical, multideck-cage morphology as a highly reversible anode material for lithium-ion batteries, Adv. Mater. 19 (2007) 993-997.

[9] P. Nithyadharseni, M.V. Reddy, B. Nalini, M. Kalpana, B.V.R. Chowdari, Sn-based intermetallic alloy anode materials for the application of lithium ion batteries, Electrochim. Acta 161 (2015) 261-268.

[10] H.G. Zhang, T. Shi, D.J. Wetzel, R.G. Nuzzo, P.V. Braun, 3D scaffolded nickel-tin Li-ion anodes with enhanced cyclability, Adv. Mater. 28(4) (2016) 742-747.

[11] J.S. Cho, Y.C. Kang, Nanofibers comprising yolk-shell Sn@void@SnO/SnO_2 and hollow SnO/SnO_2 and SnO_2 nanospheres via the Kirkendall diffusion effect and their electrochemical properties, Small 11(36) (2015) 4673-4681.

[12] L. Huang, H.B. Wei, F.S. Ke, X.Y. Fan, J.T. Li, S.G. Sun, Electrodeposition and lithium storage performance of three-dimensional porous reticular Sn-Ni alloy electrodes, Electrochim. Acta 54 (2009) 2693-2698.

[13] S.R. Gowda, A.L.M. Reddy, X.B. Zhan, H.R. Jafry, 3D nanoporous nanowire current collectors for thin film microbatteries, Nano Lett. 12(3) (2012) 1198-1202.

[14] Y.H. Xu, Q. Liu, Y.J. Zhu, Y.H. Liu, A. Langrock, M.R. Zachariah, C.S. Wang, Uniform nano-Sn/C composite anodes for lithium ion batteries, Nano Lett. 13(2) (2013) 470-474.

[15] P.L. Taberna, S. Mitra, P. Simon, P. Poizot, J.-M. Tarascon, High rate capabilities Fe_3O_4-based Cu nano-architectured electrodes for lithium-ion battery applications, Nat. Mater. 5(7) (2006) 567-573.

[16] B.D. Polat, O. Keles, The use of well-aligned composite nanorod arrays as anode material for lithium rechargeable batteries, J. Power Sources 266(1) (2014) 353-364.

[17] Z.L. Chen, R.B. Wu, H. Wang, Y.K. Jiang, L. Jin, Y.H. Guo, Y. Song, F. Fang, D.L. Sun, Construction of hybrid hollow architectures by in-situ rooting ultrafine ZnS nanorods within porous carbon polyhedra for enhanced lithium storage properties, Chem. Eng. J. 326 (2017) 680-690.

[18] Y. Wang, J.Y. Lee, H.C. Zeng, Polycrystalline SnO_2 nanotubes prepared via infiltration casting of nanocrystallites and their electrochemical application, Chem. Mater. 17(15) (2005) 197-208.

[19] C.R. Zhu, X.H. Xia, J.L. Liu, Z.X. Fan, D.L. Chao, H. Zhang, H.J. Fan, TiO_2 nanotube@SnO_2 nanoflake core-branch arrays for lithium-ion battery anode, Nano Energy 4 (2014) 105-112.

[20] X. Zhou, L. Yu, X.W. Lou, Encapsulating Sn nanoparticles in amorphous carbon nanotubes for enhanced lithium storage properties, Adv. Energy Mater. 6(22) (2016) 1601177.

[21] J.M. Kim, Y.S. Huh, H.J. Kim, K.G. Song, S.H. Kim, H.S. Park, Hollow triple-shelled SiO_2/TiO_2/polypyrrole nanospheres for enhanced lithium storage capability, Chem. Eng. J. 237 (2014) 380-386.

[22] Y.L. Ding, Y. Wen, P.A. Aken, Large-scale low temperature fabrication of SnO_2 hollow/nanoporous nanostructures: the template engaged replacement reaction mechanism and high-rate lithium storage, Nanoscale 6(19) (2014) 1141-11418.

[23] Y.P. Tang, H.N. Zhang, J.Q. Li, G.G. Hou, H.Z. Cao, L.K. Wu, G.Q. Zheng, Q.L. Wu, Three-dimensional ordered macroporous Cu/Fe_3O_4 composite as binder-free anode for lithium-ion batteries, J. Alloys Compd. 719 (2017) 203-209.

[24] S.Z. Kure-Chu, A. Satoh, S. Miura, H. Yashiro, Nanoporous Sn-SnO_2-TiO_2 composite films electrodeposited on Cu sheets as anode materials for lithium-ion batteries, J. Electrochem. Soc. 162(7) (2015) D305-D311.

[25] J. Liu, Y. Wen, P.V. Aken, J. Maier, Y. Yu, Facile synthesis of highly porous Ni-Sn intermetallic microcages with excellent electrochemical performance for lithium and sodium storage, Nano Lett. 14(11) (2014) 6387.

[26] K. Zhuo, M.G. Jeong, C.H. Chung, Highly porous dendritic Ni-Sn anodes for lithium-ion batteries, J. Power Sources 244 (2013) 601-605.

[27] H. Zhang, M.R. Zhang, M.L. Zhang, L. Zhang, A.P. Zhang, Y.M. Zhou, P. Wu, Y.W. Tang, Hybrid aerogel-derived Sn-Ni alloy immobilized within porous carbon/graphene dual matrices for high-performance lithium storage, J. Colloid Inter. Sci. 501(2017) 267-272.

[28] H. Groulta, H.E. Ghallali, A. Barhounc, E. Briota, C.M. Julien, F. Lantelmea, S. Borensztjand, Study of Co-Sn and Ni-Sn alloys prepared in molten chlorides and used as negative electrode in rechargeable lithium battery, Electrochim. Acta 56 (2011) 2656-2664.

[29] J. Hassoun, S. Panero, P. Simon, P. Taberma, B. Scrosati, High-rate, long-life Ni-Sn nanostructured electrodes for lithium-ion batteries, Adv. Mater. 38(35) (2010) 1632-1635.

[30] Z. Edfoufa, C.F. Georgesa, F. Cuevasa, M. Latrochea, T. Hezequeb, G. Caillonb, C. Jordy, M.T. Sougrati, J.C. Jumas, Nanostructured $Ni_{3.5}Sn_4$ intermetallic compound:

An efficient buffering material for Si-containing composite anodes in lithium ion batteries, Electrochim. Acta 89 (2013) 265-371.

[31] M. Tian, W. Wang, Y.j. Wei, R. Yang, Stable high areal capacity lithium-ion battery anodes based on three-dimensional Ni-Sn nanowire networks, J. Power Sources 211 (2012) 46-51.

[32] W.B. Liu, C.L. Xin, L. Chen, J.Z. Yan, N. Li, S.Q. Shi, S.C. Zhang, A facile one-pot dealloying strategy to synthesize monolithic asymmetry-patterned nanoporous copper ribbons with tunable microstructure and nanoporosity, RSC Adv. 6 (2016) 2662-2670.

[33] W.B. Liu, S.C. Zhang, N. Li, J.W. Zheng, S.S. An, G.X. Li, Influence of dealloying solution on the microstructure of monolithic nanoporous copper through chemical dealloying of Al 30 at.% Cu alloy, Int. J. Electrochem. Sci. 7 (2012) 7993-8006.

[34] W.B. Liu, P. Cheng, J.Z. Yan, N. Li, S.Q. Shi, S.C. Zhang, Temperature-induced surface reconstruction and interface structure evolution on ligament of nanoporous copper, Sci. Rep. 8 (2018) 447.

[35] W.B. Liu, S.C. Zhang, N. Li, J.W. Zheng, S.S. An, Y.L. Xing, Monolithic nanoporous copper ribbons from Mg-Cu alloys with copper contents below 33 at.%: Fabrication, structure evolution and coarsening behavior along the thickness direction, Int. J. Electrochem. Sci. 6 (2011) 5445-5461.

[36] M.J. Williamson, R.M. Tromp, P.M. Vereecken, R. Hull, F.M. Ross, Dynamic microscopy of nanoscale cluster growth at the solid-liquid interface, Nat. Mater. 2(8) (2003) 532-536.

[37] U. Lačnjevac, B.M. Jović, V.D. Jović, Electrodeposition of Ni, Sn and Ni-Sn alloy coatings from pyrophosphate-glycine bath, J. Electrochem. Soc. 159(5) (2012) D310-D318.

[38] W.B. Liu, S.C. Zhang, N. Li, J.W. Zheng, Y.L. Xing, A facile one-pot route to fabricate nanoporous copper with controlled hierarchical pore size distributions through chemical dealloying of Al-Cu alloy in an alkaline solution, Micropor. Mesopor. Mater. 138 (2011) 1-7.

[39] M. Uysal, T. Cetinkaya, A. Alp, H. Akbulut, Active and inactive buffering effect on the electrochemical behavior of Sn-Ni/MWCNT composite anodes prepared by pulse electrodeposition for lithium-ion batteries, J. Alloys Compd. 645(2) (2015) 235-242.

Figure Captions:

Figure 1. Schematic preparation processes of 3D-HP Sn-Ni and 2D-NP Sn-Ni alloys.

Figure 2. SEM images of surface morphology of as-prepared (a, b) 3D NPC substrate, (c, d) 3D-HP Sn-Ni and (e, f) 2D-NP Sn-Ni electrodes, in which parts b, d and f are the high-magnification images. The insets in parts a and e are the typical digital pictures of 3D NPC and 2D CF substrates, respectively. The insets in parts c and f are the EDX results corresponding to surface morphology of 3D-HP Sn-Ni and 2D-NP Sn-Ni electrodes, respectively. The inset in part d shows the locally enlarged image marked by the dotted white frame. Scale bar: 10 nm. (e, f) TEM and HRTEM images of hierarchical porous structure of the 3D-HP Sn-Ni electrode.

Figure 3. XRD patterns of (a) 3D NPC substrate, (b) 3D-HP Sn-Ni and (c) 2D-NP Sn-Ni electrodes.

Figure 4. The CVs recorded on the (a) 2D CF and (b) 3D NPC substrates with the sweep rate of 10 mV/s from -0.4 to -1.4 V(vs. SCE) in the 100 mL solutions containing (1) $NiCl_2 \cdot 6H_2O$ 14.67 g/L, $SnCl_2 \cdot 2H_2O$ 46 g/L, $C_4O_6H_4KNa$ 8 g/L, $K_4P_2O_7$ 300 g/L, and glycine 8 g/L; (2) $NiCl_2 \cdot 6H_2O$ 14.67 g/L, $C_4O_6H_4KNa$ 8 g/L, $K_4P_2O_7$ 300 g/L, and glycine 8 g/L; (3) $SnCl_2 \cdot 2H_2O$ 46 g/L, $C_4O_6H_4KNa$ 8 g/L, $K_4P_2O_7$ 300 g/L, and glycine 8 g/L.

Figure 5. (a) CVs of 3D-HP Sn-Ni electrode ranging from 0.01-1.5 V versus Li/Li^+ at a scan rate of 0.1 mV s^{-1}. (b) Voltage vs. capacity profiles of 3D-HP Sn-Ni electrode at a current density of 0.1 mA cm^{-2}. (c) Cycle performance curves of 3D-HP Sn-Ni and

2D-NP Sn-Ni electrode at a current density of 0.1 mA cm^{-2}. (d) Rate capacity profiles of 3D-HP Sn-Ni electrode at different current densities of 0.1, 0.2, 0.3, 0.4 mA cm^{-2}.

Figure 6. Nyquist plots of (a) 3D-HP Sn-Ni electrode before cycling and after 50 and 200 cycles and (b) 2D-NP Sn-Ni electrode before cycling and after 50 cycles, respectively. The insets in parts a and b show the corresponding high frequency zones at a higher magnification.

Figure 7. SEM images of (a) 2D-NP Sn-Ni electrode after 50 charge-discharge cycles and (b, c) 3D-HP Sn-Ni electrode after 50 and 200 charge-discharge cycles at the current density of 0.1 mA cm^{-2}. The insets show locally magnified images marked by the dotted white rectangles. Scale bar: 500 nm)

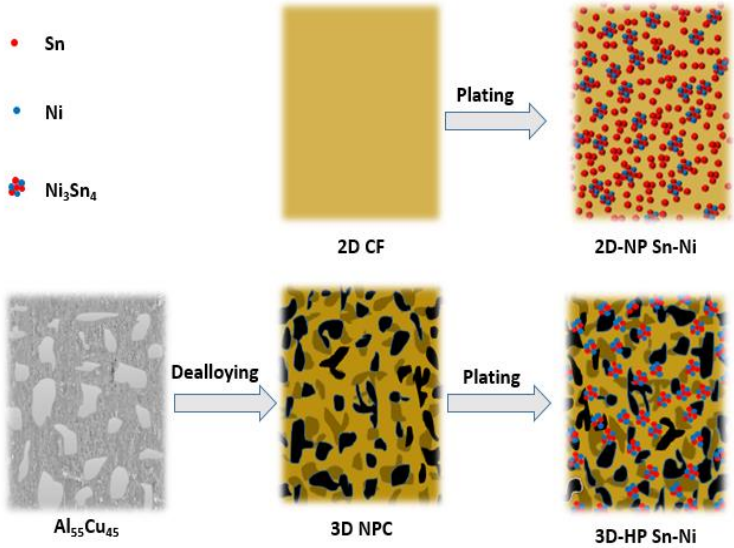
Sn
Ni
Ni_3Sn_4
2D CF
Plating
2D-NP Sn-Ni
$Al_{55}Cu_{45}$
Dealloying
3D NPC
Plating
3D-HP Sn-Ni

Figure 1.

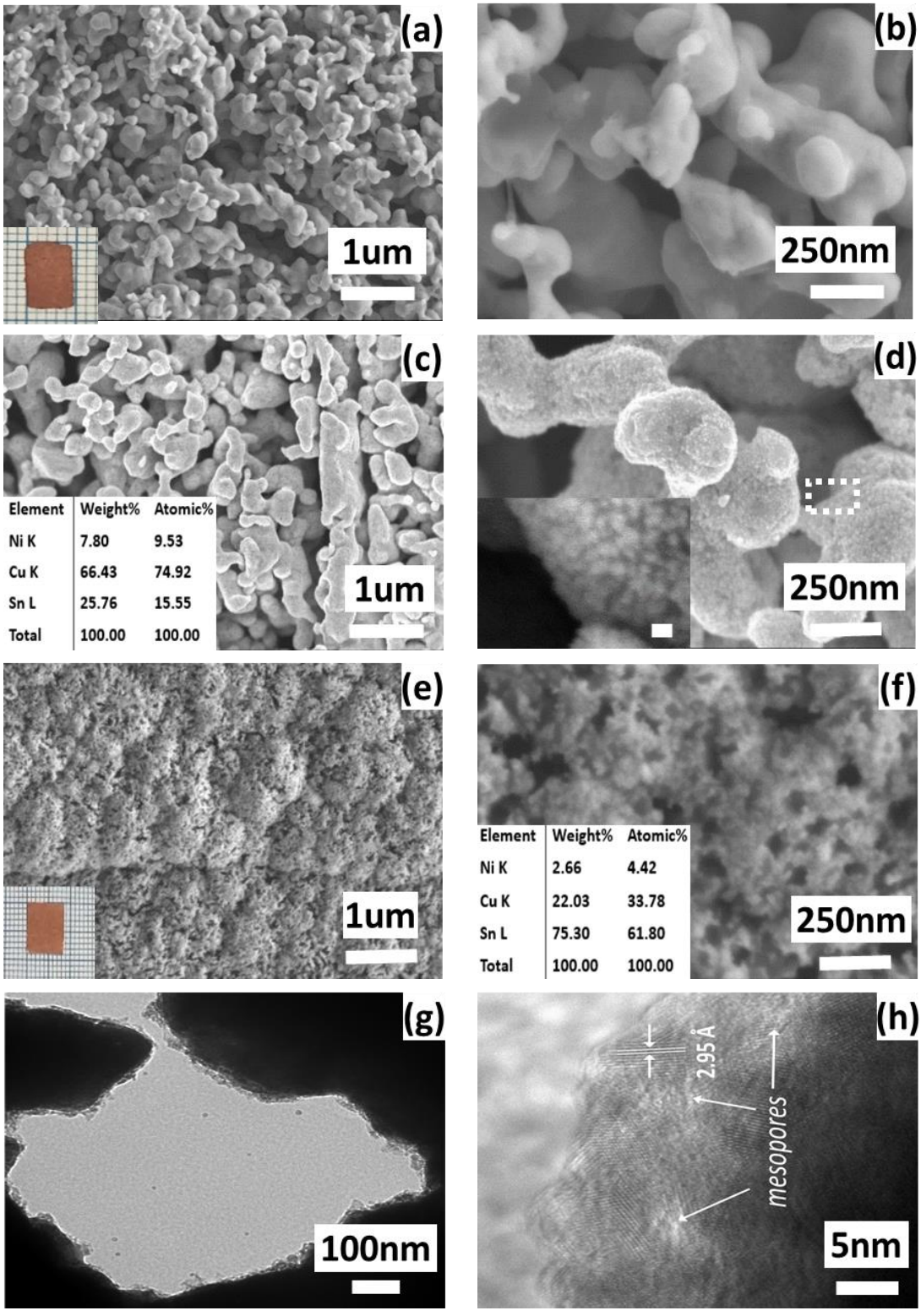
(a)
1um
(b)
250nm
(c)
Element Weight% Atomic%
Ni K 7.80 9.53
Cu K 66.43 74.92
Sn L 25.76 15.55
Total 100.00 100.00
1um
(d)
250nm
(e)
1um
(f)
Element Weight% Atomic%
Ni K 2.66 4.42
Cu K 22.03 33.78
Sn L 75.30 61.80
Total 100.00 100.00
250nm
(g)
100nm
(h)
2.95 Å
mesopores
5nm

Figure 2.

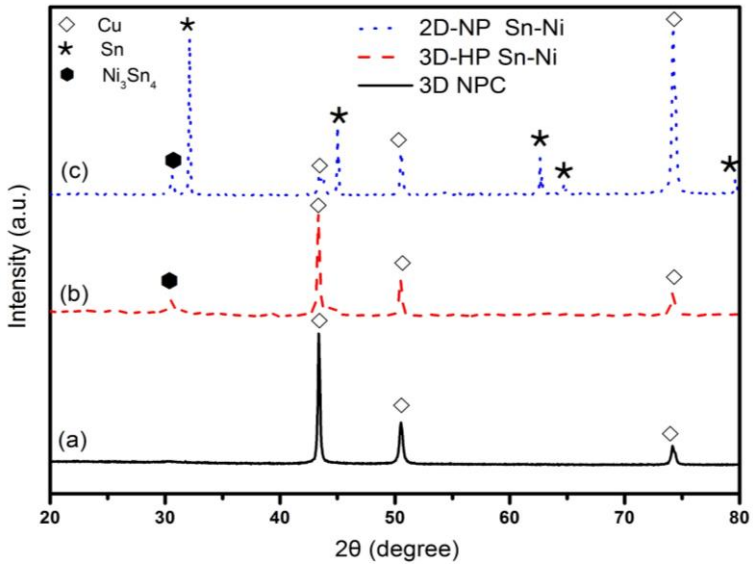
Cu
Sn
Ni3Sn4
2D-NP Sn-Ni
3D-HP Sn-Ni
3D NPC
(c)
(b)
(a)
Intensity (a.u.)
20
30
40
50
60
70
80
2θ (degree)

Figure 3.

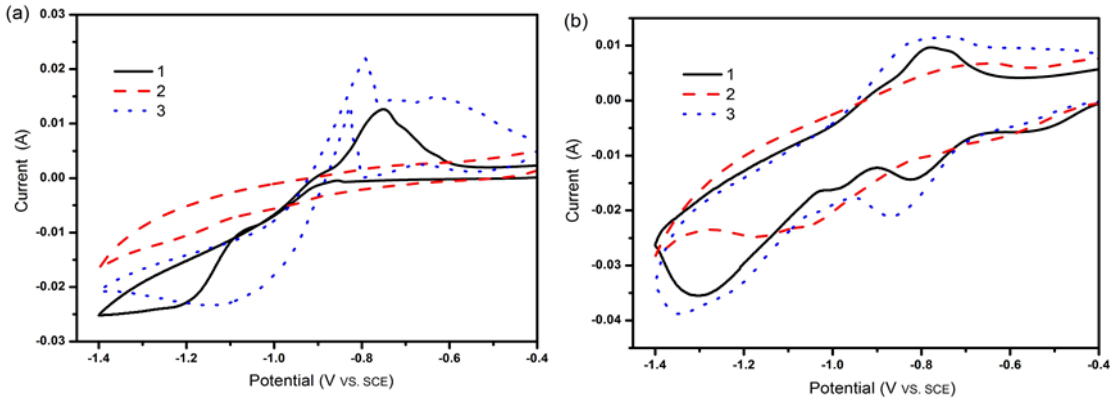

Figure 4.

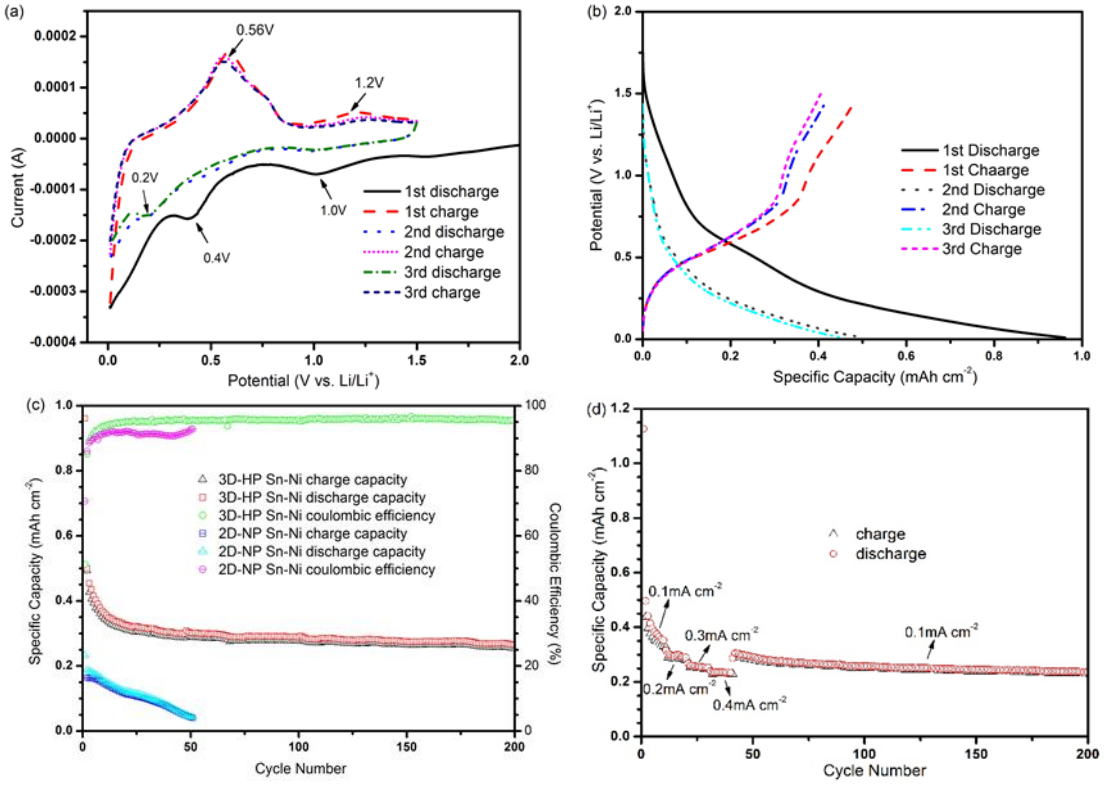
(a)
0.56V
1.2V
0.2V
1.0V
0.4V
1st discharge
1st charge
2nd discharge
2nd charge
3rd discharge
3rd charge
Current (A)
Potential (V vs. Li/Li+)
(b)
1st Discharge
1st Chaarge
2nd Discharge
2nd Charge
3rd Discharge
3rd Charge
Potential (V vs. Li/Li+)
Specific Capacity (mAh cm-2)
(c)
3D-HP Sn-Ni charge capacity
3D-HP Sn-Ni discharge capacity
3D-HP Sn-Ni coulombic efficiency
2D-NP Sn-Ni charge capacity
2D-NP Sn-Ni discharge capacity
2D-NP Sn-Ni coulombic efficiency
Specific Capacity (mAh cm-2)
Coulombic Efficiency (%)
Cycle Number
(d)
charge
discharge
0.1mA cm-2
0.3mA cm-2
0.2mA cm-2
0.4mA cm-2
0.1mA cm-2
Specific Capacity (mAh cm-2)
Cycle Number

Figure 5.

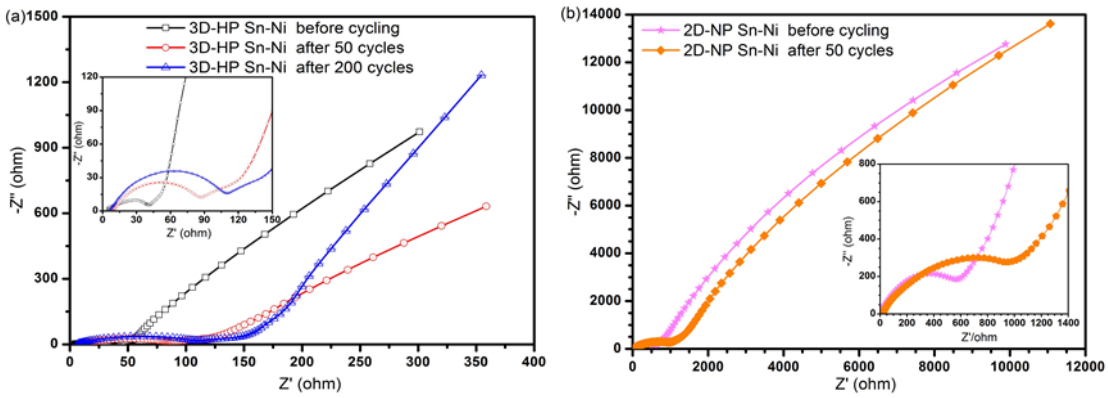
(a)
3D-HP Sn-Ni before cycling
3D-HP Sn-Ni after 50 cycles
3D-HP Sn-Ni after 200 cycles
-Z'' (ohm)
Z' (ohm)
(b)
2D-NP Sn-Ni before cycling
2D-NP Sn-Ni after 50 cycles
-Z'' (ohm)
Z' (ohm)
Z'/ohm

Figure 6.

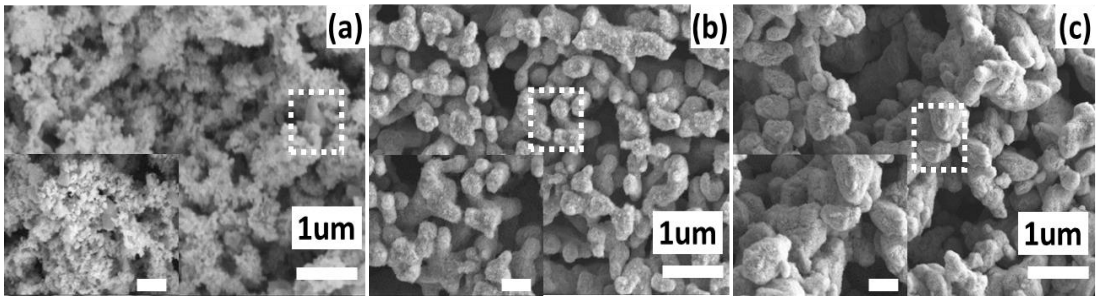

Figure 7.